ADVANCED MATERIALS
www.advmat.de

Decoupling the Failure Mechanism of 360 Wh kg^{-1} Lithium-Ion Pouch Cell During Overcharging

Shuwei Li, Yi Wang, Anxing Zhou, Zhonghao Li, Guanghai Chen, Qi Yang, Wenjun Li, Huigen Yu, Xuebing Chen, Yuanxi Wang, Liquan Chen, Zhaoxiang Wang, Hong Li, and Xuefeng Wang**

Increasing the energy density of lithium-ion batteries (LIBs) raises safety risks. Understanding failure mechanisms, especially during abuse, is essential for improved battery design and management. In this study, multiscale characterization techniques are employed to systematically investigate the overcharge behavior (from 100% to 130% state of charge) of a 360 Wh kg^{-1} pouch cell with Ni-rich cathode and SiO_x@Graphite anode. Further decoupling elucidates that the primary failure mechanism is the interfacial and structural degradation of the anode, including lithium plating on graphite, volume expansion and crack propagation in SiO_x particles, and continuous reconstruction of the solid electrolyte interphase (SEI) film, which are further promoted by dissolved Ni ions (the Ni content on the anode increases from 0.005% to 0.268% after overcharging to 5.25 V) and by released oxygen species from the Ni-rich cathode. Ni ions (mainly as Ni^{2+}) accumulate on Li-plating areas on graphite. These crosstalk reactions significantly influence the stability of both electrodes, causing severe phase transition (from LiC_6 to LiC_{12} on the anode and from layered to rock-salt phase on the cathode), continuous electrolyte decomposition and harmful gas evolution, which accelerates full-cell failure. These findings can provide guidance for the optimization of battery safety management systems.

1. Introduction

The rapid growth of lithium-ion batteries (LIBs) in the electrochemical energy storage market is a powerful strategy for alleviating the energy crisis.[1,2] In the drive to accelerate green development, high-energy, safe LIBs are the shared expectation of both scientific research and industry.[3,4] There is an urgent need for electrochemical cells that surpass the capabilities of current LIBs, as the energy densities of conventional formats (with $LiCoO_2$/$LiFePO_4$ cathodes and graphite anodes) have reached their practical limits (250–280 Wh kg^{-1}[5]/180–210 Wh kg^{-1}).[6,7] Alternatively, high-voltage and high-capacity Ni-rich layer oxide $LiNi_xCo_yMn_{1-x-y}O_2$ (NCM, $x \geq 0.8$) cathodes coupled with high-capacity Si-based anodes (e.g., SiO_x) are considered one of the most promising candidates with energy density exceeding 400 Wh kg^{-1}, which are highly attractive for numerous commercial products, from portable consumer electronics to electric vehicles.[8–11] However, the practical integration of these high-capacity materials faces critical challenges.

Ni-rich cathodes suffer from oxygen release and transition metal (TM) dissolution,[12–14] while Si-based anodes endure significant volume expansion and continuous solid electrolyte interphase (SEI) reconstruction.[15–17] These side reactions result in the gradual consumption of active materials and gas accumulation within the battery, which in turn significantly increases internal pressure, accelerates aging, disrupts normal charging/discharging, and can cause overcharging.[18] Moreover, the practical application environment and charging protocols are complex, and these intrinsic limitations are exacerbated in high-energy full-cell configurations, particularly under abusive operational conditions such as overcharging. The synergistic degradation mechanisms, including crosstalk and interfacial instability, accelerate the capacity fade and increase the thermal runaway risks.[19–21] A deep understanding of this complex interplay of material-level limitations and system-level interactions is the basis for large-scale commercial applications of high-energy LIBs.

In practical production, the improvement of battery energy density inevitably leads to a compromise in safety.[4,22,23] Overcharging stands as one of the primary causes of thermal runaway in LIBs and remains one of the most prevalent safety concerns in current applications.[21,24] Particularly in battery packs, inconsistencies in capacity and internal resistance gradually arise due

S. Li, A. Zhou, L. Chen, Z. Wang, H. Li, X. Wang
Beijing National Laboratory for Condensed Matter Physics
Institute of Physics
Chinese Academy of Sciences
Beijing 100190, China
E-mail: hli@iphy.ac.cn; wxf@iphy.ac.cn

S. Li, Y. Wang, Z. Li, X. Chen, Y. Wang
Tianmu Lake Institute of Advanced Energy Storage Technologies Co. Ltd.
Liyang, Jiangsu 213300, China

G. Chen, Q. Yang, W. Li, H. Yu
Beijing Welion New Energy Technology Co., Ltd.
Beijing 102402, China

The ORCID identification number(s) for the author(s) of this article can be found under https://doi.org/10.1002/adma.202518298

DOI: 10.1002/adma.202518298

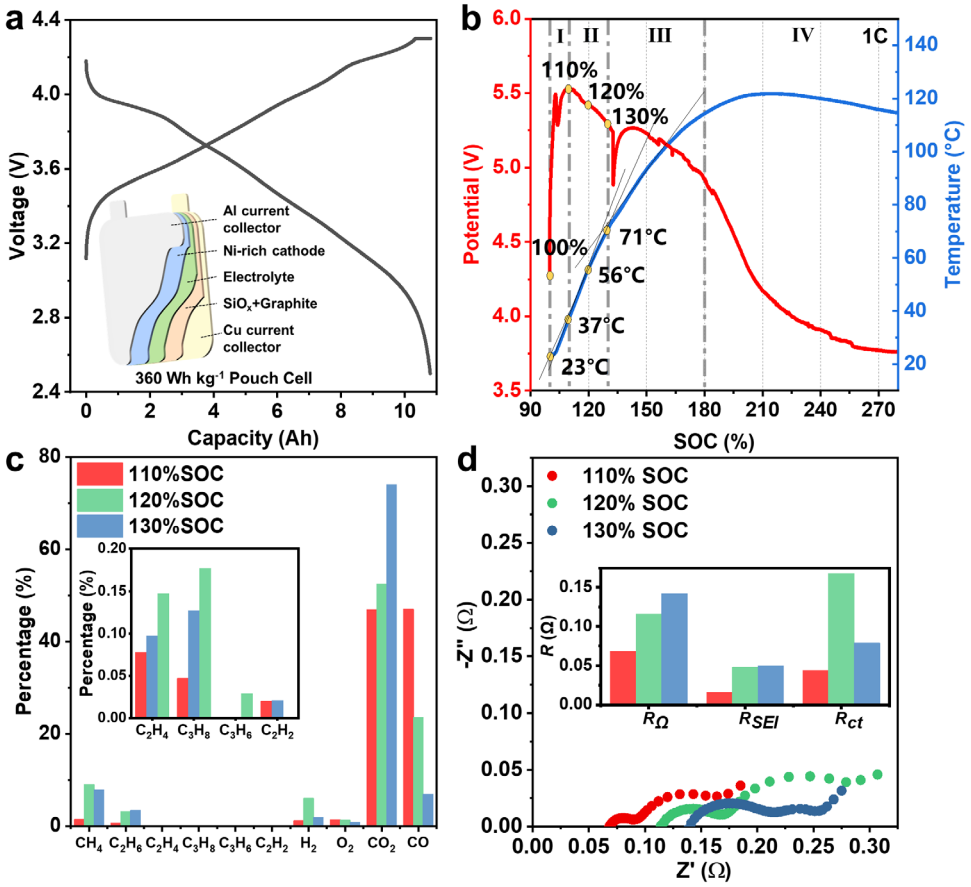

Figure 1. The overcharged behavior of a pouch cell using a Ni-rich cathode and SiO_x@Gr anode. a) The voltage profile cycled between 2.5 and 4.3 V at 10 A, and the internal structure of the pouch cell. b) The voltage and temperature changes during the overcharge process. c) The concentration and species evolution of released gases and d) the EIS spectra at 110%, 120%, and 130%SOC. The inset in d) shows the fitting results of EIS.

to manufacturing variations, usage conditions, and uneven temperature distribution, significantly increasing the likelihood of overcharging.[25,26] Previous work[27,28] revealed that even slight overcharging (100% < state of charge (SOC) < 120%) can profoundly compromise thermal safety. During overcharging, the unstable interface undergoes continuous uncontrolled growth driven by potential and temperature fluctuations, triggering interface failure, thus leading to active lithium loss, electrolyte depletion and increased impedance.[29] As the interfacial degradation progresses, structural damage to the cathode and lithium plating on the anode emerge.[8,17] In severe cases, intensified internal reactions generate substantial gas at interfaces, causing rapid temperature and pressure surges.[13,30] These conditions may induce internal short circuits, ultimately leading to battery failure.

While extensive studies[22,24,27,28,31,32] have focused on the thermal behavior and failure mechanisms of graphite-based LIBs during overcharging, critical knowledge gaps remain regarding the structural and interfacial evolution of Ni-rich/Si-based full-cells under overcharge conditions. Moreover, there are few studies on the degradation mechanism caused by dynamic overcharging, and the degradation mechanism during different-level overcharging has not been fully elucidated.[33,34] In addition, current research primarily focuses on thermal runaway thresholds and voltage/temperature profiles,[27,32] or the degradation pathways of Ni-rich cathodes[12,35,36] and Si-based anodes at the material level, with little attention given to the interface evolution mechanisms and interactions between different interfacial reactions in pouch-type full-cells. Therefore, a comprehensive understanding of the failure mechanism is essential for developing mitigation strategies to enhance the safety and durability of high-energy Ni-rich/Si-based batteries.

In this work, we present a multiscale investigation into the structural and interfacial degradation mechanisms of a 360 Wh kg^{-1} pouch cell comprising a Ni-rich cathode ($LiNi_{0.9}Co_{0.07}Mn_{0.03}O_2$, NCM90, ≈230 mAh g^{-1}) and SiO_x@Gr (30%SiO_x+70%Graphite, ≈650 mAh g^{-1}) anode during overcharging. The characterizations by cross-section polisher (CP)-scanning electron microscopy (SEM), cryogenic high-resolution transmission electron microscopy (cryo-HRTEM) and time-of-flight secondary-ion mass spectrometer (ToF-SIMS) confirm that the main cause of the performance failure of the pouch cell during overcharging is the structural degradation of the SiO_x@Gr anode, including Li plating on graphite, and crack propagation in SiO_x particles. The elevated overcharging exacerbates the thickening of the rock-salt phase on the surface and the emergence of intergranular cracks in the bulk of the Ni-rich cathode, promoting Ni^{2+} dissolution. The dissolved Ni^{2+} ions migrate to the

anode, catalyzing electrolyte decomposition and the formation of LiF-rich SEI. Such crosstalk also alters the gas release and adversely affects performance in the pouch cells at various overcharge states. Our findings provide fundamental insights into the failure mechanisms of NCM90||SiO_x@Gr full cell under abusive conditions and give guidance for the optimal design of safer cells and the optimization of battery safety management systems.

2. Results and Discussion

2.1. The Evolution of the Full Cell During the Overcharge Process

The 360 Wh kg^{-1} pouch cell used in this work consisted of a Ni-rich ternary layered transition metal oxide (NCM90) cathode, a SiOx@Gr anode, and a commercial electrolyte system. Detailed information and parameters of the pouch cell are provided in Table S1 (Supporting Information). The voltage profile of the pouch cell after formation (**Figure 1a**) shows an initial reversible capacity of ≈10.8 Ah between 2.5 and 4.3 V at 10 A. Figure 1b illustrates the evolution of the battery voltage and temperature from the beginning of the overcharge process to the thermal runaway. According to the literature[32] and the observed voltage variation, the whole overcharge process for the NCM90||SiO_x@Gr battery can be divided into four stages: (1) During Stage I (from 100%SOC to 110%SOC), the battery voltage increases rapidly but the temperature begins to rise from 23 to 37 °C at a slow rate due to heat generation from side reactions; (2) During Stage II (from 110%SOC to 130%SOC), the temperature still shows continuous growth from 37 to 71 °C. However, the voltage peaks at ≈5.5 V and then drops, which is consistent with the occurrence of micro-shorting,[37,38] (3). During Stage III (from 130%SOC to 180%SOC), the voltage shows a steady drop and the temperature rises steadily, and the battery starts to swell obviously. (4) During stage IV (>180%SOC), the battery ruptures as the inner pressure exceeds its limit, resulting in the deformation of the separator, internal short circuit and thermal runaway. Table S2 (Supporting Information) summarizes the characteristics of each stage during the overcharging process.

In consideration of the practical application scenario of the commercial pouch batteries, we chose 110%, 120%, and 130%SOC samples for further investigation. The gas release during the overcharge process was captured by gas chromatography (GC). Figure 1c shows that much CO_2 and CO, along with a small amount of combustible gas such as CH_4, C_2H_6 and H_2 is released at 110%SOC, although the measured battery temperature is only 37 °C at this stage. At high voltages, Ni-rich cathodes release reactive oxygen species such as singlet oxygen ($^1O_2$), superoxide (O_{2-}), and/or peroxide (O_2^{2-}), which can oxidize cyclic carbonate solvents like ethylene carbonate (EC), giving rise to gaseous products including CO_2 and CO.[39,40] In addition, the oxidation of the carbon black[41] and the decomposition of electrolyte[42] and SEI[43] can also result in CO_2 release. The evolution of some alkane gases, such as CH_4, C_2H_6, was mainly derived from the reductive decomposition of chain-structured carbonate solvents from the anode side.[36] The reductive decomposition of EC leads to the evolution of C_2H_4.[13,30] The concentration of various carbonaceous gases increased with higher temperature and SOC, while the concentration of H_2 first climbed up and then declined. The origin of the enhanced H_2 evolution was the diffusion of protic electrolyte oxidation species (R-H^+) from the cathode to the anode and their subsequent reduction, especially for high charging potential (more oxidation for electrolyte), elevated temperature (SEI is unstable) or the crossover catalysis of the dissolved Ni ions.[44,45] However, the concentrations of O_2 and CO declined as the battery was overcharged to a higher SOC, probably suggesting the reaction between CO and O_2 to form CO_2 at high temperatures. Meanwhile, the decomposition of electrolyte and SEI accelerates at elevated temperature, generating a large amount of CO_2 gas. Batteries at 100%SOC were stored at 55 °C for 7 days to isolate the thermal contribution from over-delithiation/lithiation effects (Figure S1, Supporting Information). Negligible gas release in fully charged cells after high-temperature storage demonstrates that gas generation observed during overcharging from 100% to 130%SOC is predominantly attributed to intense interfacial reactions at electrode-electrolyte interfaces driven by elevated voltage.

Electrochemical impedance spectra (EIS) of pouch cells at different SOC (Figure 1d) and corresponding equivalent circuit model (Figure S2, Supporting Information) and fitting results (Table S3, Supporting Information) exhibit a growing resistance to Li^+ transport through the SEI (R_{SEI}) from 0.016Ω at 110%SOC to 0.050Ω at 130%SOC, as well as the resistance of charge transfer (R_{ct}). The above observation of the whole battery during overcharge process indicates the severe structural and performance degradation of the SiO_x@Gr anode and NCM90 cathode after overcharging. According to the variation in the voltage and temperature behavior (Figure 1b; Figure S3, Supporting Information), it is representative to choose samples at 100%, 110%, and 130%SOC to uncover its underlying degradation mechanism.

2.2. The Evolution of the SiO_x@Gr Anode During the Overcharge Process

The pouch cells with 100%, 110%, and 130%SOC were disassembled in the glove box, and the corresponding optical images are shown in Figure S4 (Supporting Information). With the increasing severity of overcharge conditions, a discernible darkening phenomenon is observed on the anode and separator, accompanied by a significant enlargement of the dark spot formations, whereas the cathode exhibits no significant alterations. The X-ray diffraction (XRD) shows that the relative intensity of the LiC_{12} peak gradually increases from 100%SOC to 130%SOC, especially in the black area of the 130%SOC anode (130%SOC-B) (Figure S5, Supporting Information), suggesting the loss of active Li^+ from the lithiated graphite.[46] SEM was applied to observe the morphology change of the SiO_x@Gr anode at different SOCs (**Figure 2a–c**). After overcharging, some side-reaction products form on the surfaces of both lithiated graphite and SiO_x particles. Notably, abundant F-rich nanoparticles appeared on the 130% SOC anode particles (Figure S6b, Supporting Information), which suggests that the continuous decomposition of F-containing electrolyte under overcharging generates more LiF.[47] In addition, there were some crisscrossed cracks on the surface of the lithiated SiO_x particles (Figure 2a) due to their drastic volume expansion. It is worth noting that some rod-like particles with several hundred nanometers emerge on the surface of the 110% SOC anode particles, suggesting the beginning of the Li

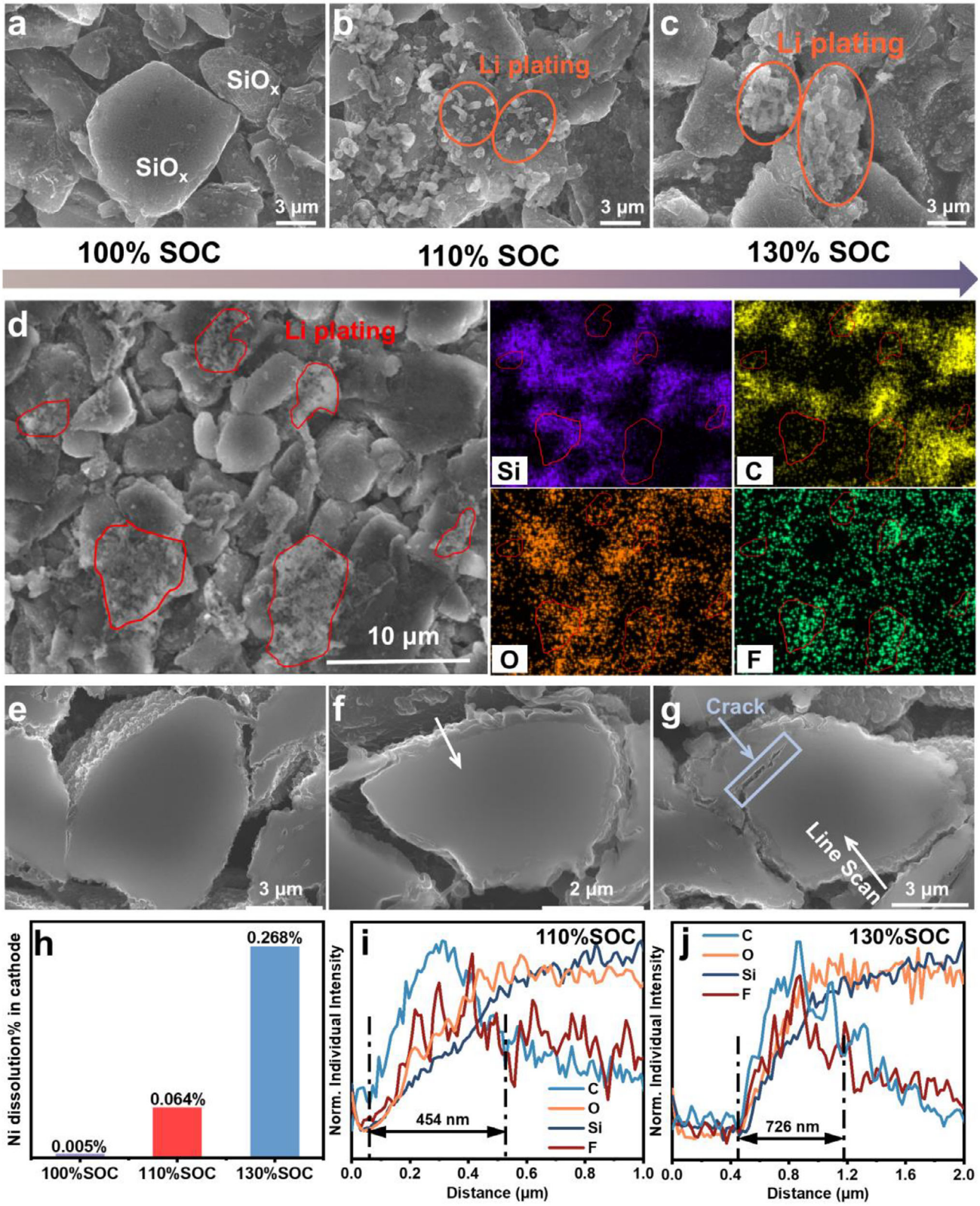

Figure 2. Morphology and structure change of the SiO_x@Gr anode at different SOCs. a–c) The SEM images of the a) 100%SOC, b)110%SOC and c) 130%SOC samples. d) The SEM image and corresponding EDS mappings of the anodes at 130%SOC. e–g) Magnified cross-sectional images of the e) 100%SOC, f) 110%SOC and g) 130%SOC samples and i,j) corresponding line scan curves based on elemental mappings. h) The proportion of dissolved Ni to total Ni in the cathode of the pouch cell at different SOCs.

plating (Figure 2b). Furthermore, the appearance of the micron-sized lithium clusters indicates the severity of lithium plating at 130%SOC (Figure 2c). As shown in Figure S7 (Supporting Information), the quantitative analysis demonstrates that the areal coverage of lithium plating on the anode rises from 1.5% to 7.7% when the SOC is elevated from 110% to 130%. The corresponding energy dispersive spectrometer (EDS) mappings results at 130%SOC (Figure 2d) reveal that the Li plating tends to take place on the surfaces of graphite particles, which results in the elemental localization of O and F. As the increase of SOC (overcharging) and the internal temperature of the battery, a portion of LiC_6 reacts with the electrolyte and converts into LiC_{12}, accompanied by an acceleration of surface parasitic reactions.

Furthermore, to directly visualize the morphology changes of the graphite and SiO_x particles, the cross-section polisher (CP) technique was applied (Figure S8, Supporting Information). After continuous overcharge, the thickness of SiO_x@Gr anode gradually expands from 108 µm (100%SOC, Figure S8a, Supporting Information) to 114 µm (110%SOC, Figure S8b, Supporting Information), then to 118 µm (130%SOC, Figure S8c, Supporting Information). The volume expansion results in loose stacking and large gaps among the particles, leading to poor contact between active material particles and hindrance of the fast charge transfer. Figure 2a–c; Figure S8d–f (Supporting Information) show that there are no obvious cracks both on the surface and inside of overcharged graphite particles. However, the surface of the SiO_x particles is subjected to continuous corrosion during the overcharge process, and visible cracks were observed in the SiO_x particles at 130%SOC (Figure 2e–g), indicating the Li^+ migration from graphite to adjacent Si particles. Based on the line scanning results acquired by EDS, the surface corrosion layer is found to consist of C, F and O, which is SEI of the SiO_x particles. The thickness of this interface progressively increases from 454 (±58) nm at 110% SOC to 726 (±123) nm at 130% SOC (Figure 2i–j; Figure S9, Supporting Information), suggesting the continuous formation and thickening of the SEI as the newly exposed surfaces react with the electrolyte during the overcharging progress.[15] Figure S10 (Supporting Information) shows a negligible increase of the thickness for the 100%SOC SiO_x@Gr anode and undetectable morphological alterations observed in either the graphite or SiO_x particles after storage at 55 °C for 7 days at 100%SOC. These findings suggest that the structural and interfacial evolution of the overcharged anode is predominantly attributable to persistent lithium intercalation and deposition.

More notably, signals of transition metal Ni ions were detected on the overcharged anode and corresponding separator (Figure S11, Supporting Information), revealing the Ni accumulation at lithium deposition sites. The results of the inductively coupled plasma optical emission spectroscopy (ICP-OES, Figure 2h; Table S5, Supporting Information) revealed that the proportion of dissolved Ni to the total Ni content in the cathode at 110% SOC (0.064%) was 12 times higher than that at the non-overcharged state (100%SOC, 0.005%). This value surged dramatically to 54-fold when overcharged to 130%SOC (0.268%). Such observations indicate that significant migration of Ni ions from the cathode to the anode occurs predominantly between 110%SOC and 130%SOC, accompanied by an accelerating decrease in full-cell voltage and an increase in internal resistance (Figure 1b–d). Dissolved Ni ions migrating to the anode can catalyze the decomposition of electrolytes and accelerate the growth of the SEI.[48]

The nanostructure of the SEI on the SiO_x@Gr anodes at different SOCs was visualized through cryo-HRTEM, electron energy-loss spectroscopy (EELS), and EDS mappings (**Figure 3a–c**; Figures S12–S15, Supporting Information). As shown in Figure 3a, the SEI on graphite particles at 100%SOC exhibits a mosaic structure with crystalline inorganic Li_2O nanograins sparsely dispersed in the amorphous organic substrates. After overcharging, more Li_2O and a few crystalline LiF nanograins are present in SEI at 110%SOC (Figure 3b), and both Li_2O and LiF nanograins were significantly increased in SEI at 130%SOC (Figure 3c). It is worth noting that some F-rich nanoparticles with a diameter in the range of 50-300 nm were either attached to the particle surfaces or detached and scattered around the particles, especially with the distribution of Ni elements, particularly observed on the graphite particles (Figure S12, Supporting Information). The EDS mapping (Figure S13, Supporting Information), EELS mappings (Figure S14a, Supporting Information) and spectra of the Li *K*-edge (Figure S14b, Supporting Information) and F *K*-edge (Figure S14c, Supporting Information) show the core-shell structure, in which the core is dominated by LiF and the shell is surrounded by the Li_2O nanograins and some amorphous organic species. The corresponding spectra of the Ni *L*-edge (Figure S14d, Supporting Information) display that the Ni deposits are mainly in the form of Ni^{2+} inside the nanoparticles on the anode at 130%SOC. These increases of the inorganic nanograins in the SEI are attributed to the continuous decomposition of the electrolyte and the conversion of organic species to inorganic species at high temperature.[29,43] In terms of the SiO_x particles, there were still some crystalline Li_2O nanograins in the interface layer on 100%SOC SiO_x particles (Figure S15a, Supporting Information). However, only several crystalline LiF nanograins were observed in the SEI at 110%SOC, and no crystalline inorganic nanograins were in the SEI at 130%SOC after overcharging, which is largely dominated by amorphous lithium silicate since organics are supposed to decompose (Figure S15b,c, Supporting Information).

The dynamic evolution of SEI thickness and composition can be systematically monitored through comparative analysis of characteristic mass spectral signatures corresponding to specific chemical constituents in ToF-SIMS depth profiles (Figure S16, Supporting Information). The SEI thickness on the graphite particle was determined by monitoring the evolution of C^- fragment counts, which was ≈15.0 nm at 100%SOC (Figure S16a, Supporting Information), expanded to ≈24.6 nm at 110%SOC (Figure S16b, Supporting Information), and further increased to 30.2 nm at 130%SOC (Figure S16c, Supporting Information). Based on the electrolyte formulation comprising specific lithium salts (e.g., $LiPF_6$, Lithium bis(fluorosulfonyl)imide (LiFSI)) and carbonate solvents, the C_2HO^- fragment and the LiF_2^-, $PO_2F_2^-$, PO_3^-, SO_3^- fragments were represented to the organic and inorganic SEI components, respectively.[14,29] The C_2HO^- fragment is produced from alkyl carbonate species that originate from the decomposition of the carbonate solvents, whereas the LiF_2^- fragment represents LiF deposits from decomposition reactions of lithium salts.[49] The $PO_2F_2^-$ and PO_3^- fragments represent the decomposition of $LiPF_6$, while the SO_3^- fragment represents the decomposition of LiFSI. Figure 3d–f and Figure S17 (Supporting

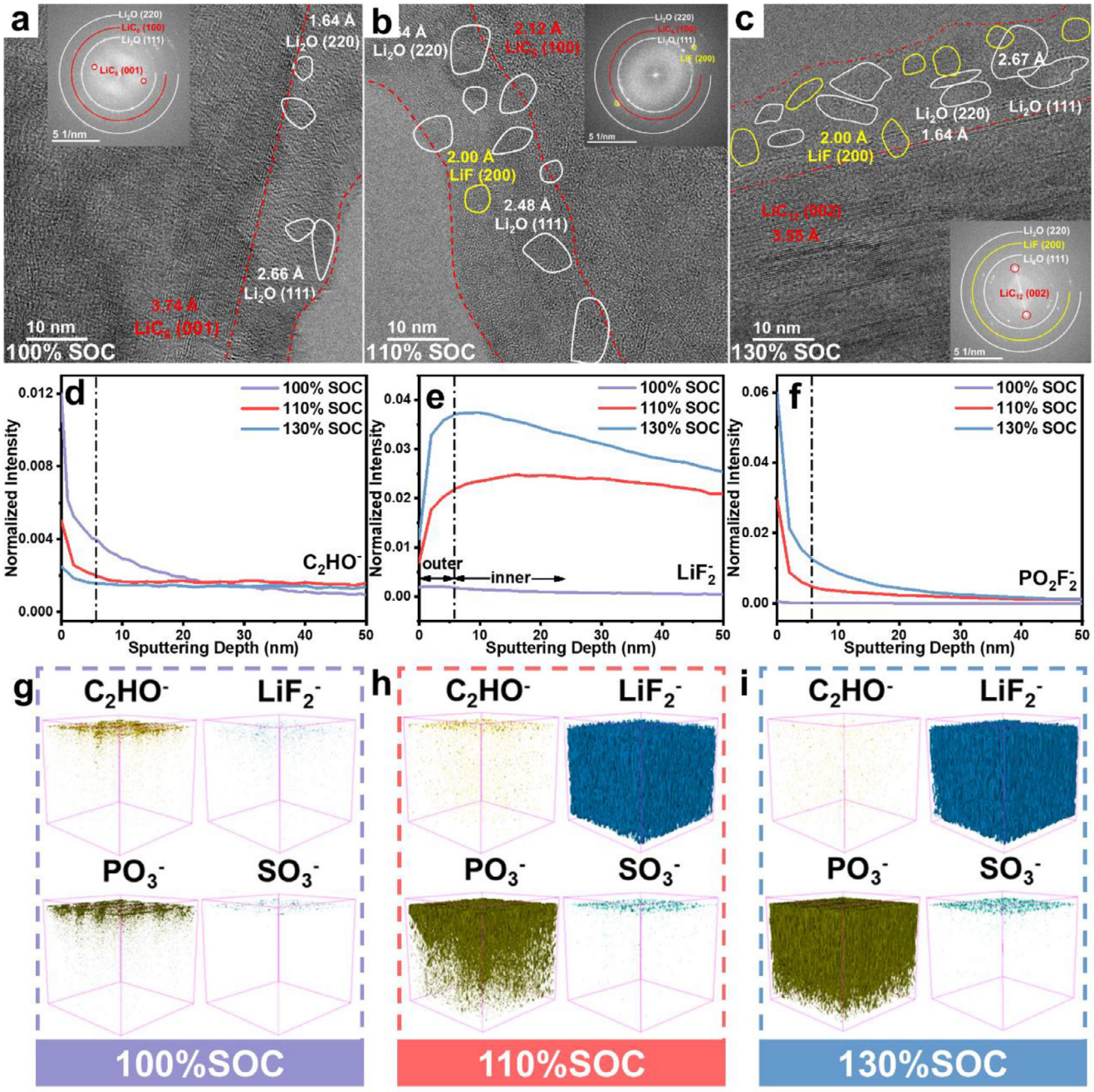

Figure 3. Nanostructural evolution of the SEI formed on the SiO_x@Gr anodes at different SOCs. a–c) Cryo-HRTEM images, d–f) normalized secondary-ion yields versus sputtering depth (nm) for the secondary ion fragments C_2HO^-, LiF_2^- and $PO_2F_2^-$, and g–i) 3D renderings for the secondary ion fragments LiF_2^-, PO_3^-, SO_3^- and C_2HO^- of the SiOx@Gr anode a), d) and g) at 100%SOC, b), e) and h) at 110%SOC, and c), (f) and (i) at 130%SOC.

Information) show the intensity evolutions of the corresponding secondary ion fragments with both SOC conditions and sputter depth progression. The intensity of the C_2HO^- fragment decreases with depth and significantly drops after overcharging (Figure 3d), especially in the outer surface, suggesting that unstable organic SEI is likely further decomposing into inorganic components.[49] In contrast, the intensity of the LiF_2^- fragment increases dramatically, and its distributions widen with depth after overcharging, indicating that more electrolyte decomposition to generate more LiF in the inner layer of SEI (Figure 3e). The PO_{3-} and LiF_{2-} fragments exhibit similar intensity evolution profiles and colocalization within the inner SEI layer (Figure 3e; Figure S17a, Supporting Information), which is attributed to a sustained decomposition of $LiPF_6$ salt and the thermal decomposition of metastable $Li_xPO_yF_z$ species to form more LiF and $Li_{(x-z)}PO_y$.[43] The intensity of other inorganic ion fragments (such as $PO_2F_2^-$ and SO_3^-) increases with the increased SOC and distributes in the outer layer, also indicating the continuous

decomposition of the $LiPF_6$ and LiFSI at high temperature after overcharging (Figure 3f; Figure S17b, Supporting Information). The distribution of organic and inorganic decomposition products was demonstrated by the 3D spatial renders in Figure 3g–i and Figure S18 (Supporting Information), which is consistent with the above elemental profile results.

Several Ni-containing ion fragments were detected by ToF-SIMS, such as Ni^+, NiO_2^-, NiF_3^- on the SEI of SiO_x@Gr anode (Figure S19, Supporting Information), showing the accumulation of Ni ions in the outer SEI layer and its intensity gradually decreases with depth. Qualitatively, there is a correlation between the distributions of deposited Ni^+ and C_2HO^- fragments (Figure S20, Supporting Information), indicating more severe decomposition of the solvent in the electrolyte on the anode at 130%SOC. This finding is consistent with the deposition of Fe ions in the form of organic compounds on the graphite anode.[50] However, the spatial distributions of PO_2F_{2-} and SO_{3-} signals (Figure S20, Supporting Information) and the enrichment of Ni^{2+} on LiF nanoparticles (Figure S12, Supporting Information) suggest that the deposited Ni ions on the SiO_x@Gr composite anode are more likely to accelerate the decomposition of the lithium salt.[51]

The surface-sensitive technique X-ray photoelectron spectroscopy (XPS) was applied to investigate the chemical bond change on the top surface of the SEI (Figure S21, Supporting Information). Notably, the increase in F content induced solely by elevated temperature (55 °C-storage for 7 days) is quite limited (7% to 9%), indicating that lithium salt decomposition is primarily voltage-driven (Figure S21a, Supporting Information). Concurrently, the gradual decrease in C content demonstrates that temperature rise is not the sole driver for the conversion of organic components to inorganic species (e.g., Li_2O, LiF) within the SEI. A continually increasing lithium intercalation promotes gas-releasing decomposition of unstable organic species in the SEI. The reduction in Si content signifies substantial SEI thickening on Si particles after overcharging, consistent with the undetectable Si^- fragments in ToF-SIMS results (Figure S16, Supporting Information). C *1s* and O *1s* spectra (Figure S21b,c, Supporting Information) reveal that, unlike the thermal decomposition of organic SEI components dominating during high-temperature storage, continuous decomposition of solvents and lithium salts driven by over-lithiation constitutes the primary cause for changes in SEI thickness and composition.

2.3. The Evolution of the NCM90 Cathode During the Overcharge Process

Although there is no significant change in the surface color of the cathode (Figure S4, Supporting Information), the internal structure of the cathode has already begun to undergo noticeable degradation. Since the NCM90 has an α-$NaFeO_2$ structure of the R $\bar{3}m$ space group, the intensity ratio of the (003) peak and (104) peak reflects the extent of the cation mixing of Li/Ni, that is, the value becomes smaller, meaning that the migration of the Ni ions to the Li layers becomes more severe. From the XRD pattern (Figure S22 and Table S6, Supporting Information) we can infer that the 130% SOC material has severe Li/Ni mixing. The cross-section of the cathode at varying SOCs was examined using SEM for direct observation of morphological changes (**Figure** 4a–f). The 100% SOC cathode remained no cracks (Figure 4a), whereas overcharging to 110% SOC induced subsurface intergranular cracking between secondary particles, extending ≈32 µm from the surface (Figure 4b). With further overcharging to 130% SOC, the propagation of intergranular crack progressed with substantially greater penetration depths (≈50 µm, Figure 4c). The magnified SEM images reveal intragranular cracking within secondary particles (Figure 4d–f). The 110%SOC cathode maintains structural integrity, but there are some radial cracks that extend from the interior (Figure 4e). The microcracks increased progressively in density and in width and propagated to the surface for the cathode at 130%SOC (Figure 4f), revealing the structural degradation of the cathode.

HRTEM and fast Fourier transformation (FFT) images were performed to estimate the range where the phase transformation occurred. The progressive increase in overcharge severity induces systematic thickening of the cation-mixing layer at the surface, exhibiting a stepwise progression from ≈2 nm (100% SOC, Figure 4g) to ≈3 nm (110% SOC, Figure 4h), then further to ≈6 nm (130% SOC, Figure 4i). The formation of the highly symmetrical rock-salt phase initiated from the surface, while the bulk region remained in the rhombohedral layered phase, which was consistent with the FFT images shown in Figure 4i. Ni-rich layered oxides exhibit irreversible phase transformation from the initial layered structure to rock-salt phases on the surface, due to the release of the oxygen lattice during deep delithiation.[52] Once the dangling oxygen atoms are released and participate in the electrolyte oxidation decomposition on the surface, transition-metal (TM) ions undergo reduction to divalent states and subsequently migrate from the octahedral site in the TM layer to the octahedral site in the Li layer. This deleterious surface reconstruction process not only consumes active lithium sites but also forms an insulating surface layer that impedes bulk lithium-ion transport kinetics.[35]

The evolution of the cathode electrolyte interphase (CEI) was revealed by XPS during overcharging (Figure S23, Supporting Information). From 100%SOC to 130%SOC, the C content decreases while the concentrations of P and Ni increase on the surface (Figure S23a, Supporting Information), and a reduction of C—O, C = O, and $ROCO_2Li$ peaks in C *1s* spectra (Figure S23b, Supporting Information), which indicate diminished organic species and accelerated decomposition of lithium salts-similar to the changes observed in the SEI on the anode. In addition, the enhanced intensity of the metal-oxygen (M–O) bond in the O *1s* spectra (Figure S23c, Supporting Information) suggests a thinner CEI layer at 130%SOC. TEM observations further reveal discernible damage in the CEI of the sample at 130%SOC (Figure 4i). Such a thinner, more uneven CEI with reduced organic content may facilitate further dissolution of Ni ions and promote persistent phase transitions at the cathode surface.[53]

The overcharged cathodes at different SOCs were assembled into coin-type half-cells to compare the cathode degradation after overcharging. The voltage profile of the NCM90 cathode (Figure S24a, Supporting Information) shows a negligible overall difference, though the discharge capacity exhibits a slight decrease (from 231.53 to 227.77 mAh g^{-1}, Figure S24b, Supporting Information) from 100%SOC to 130%SOC, implying that overcharging caused little damage to the bulk structure of the cathode. However, severe cathode surface reconstruction induces Ni-ion

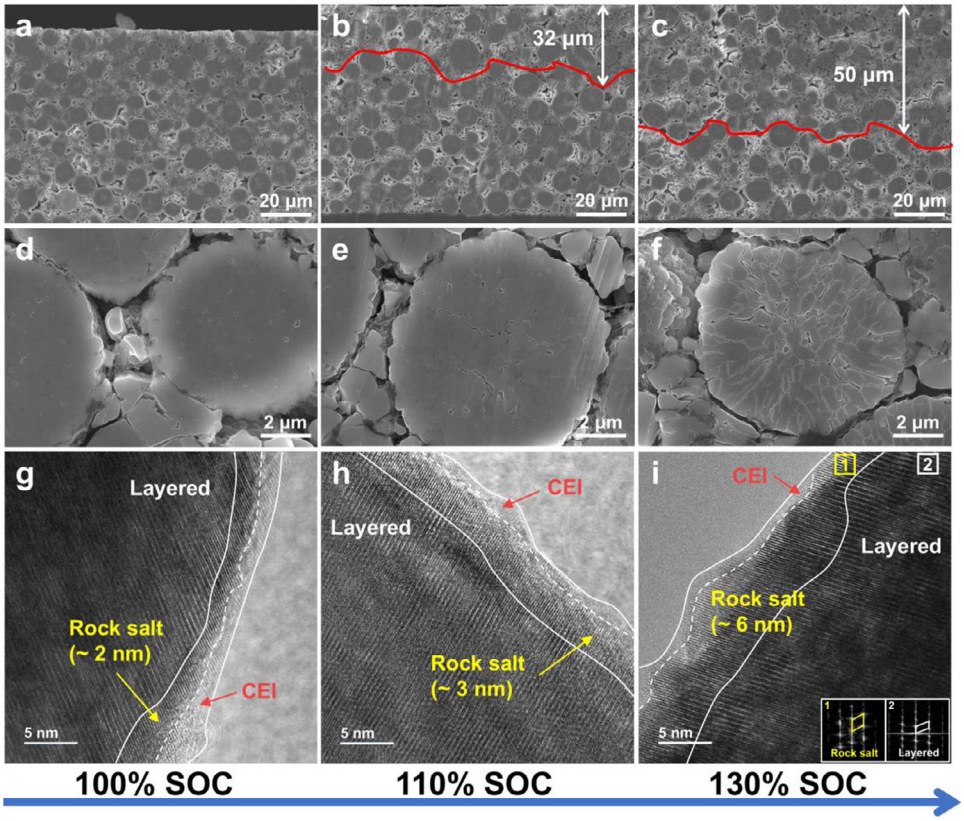

Figure 4. Morphology and structure change of the NCM90 cathode at different SOC. a–c) The cross-sectional images, d–f) corresponding magnified images and g–i) HRTEM images at a), d) and g) 100%SOC, b), e) and h) 110%SOC, and c), f) and i) 130%SOC. The corresponding FFT images of regions 1 and 2 are insert in i), respectively.

dissolution at high cut-off voltage and increases the impedance of the surface film, as evidenced by the EIS results of half-cells assembled with cathodes at different SOCs (Figure S25 and Table S7, Supporting Information). These migrating Ni ions subsequently reach the SiO_x@Gr anode, triggering decomposition of the SEI, metallic lithium deposition and gas release, ultimately leading to overcharge-induced failure of the full cell.

3. Discussion

According to the above observations, a comprehensive schematic of gas release, the nanostructure evolution of the interfaces of SiO_x@Gr anode and NCM90 cathode during the overcharge process can be proposed as shown in **Figure 5**. As the overcharge depth increases in the pouch cell, continuous extraction of Li^+ occurs from the NCM90 cathode. Severe delithiation induces microcrack propagation within the secondary particles, exacerbates Li/Ni mixing in primary particles, thickens the surface reconstruction layer, and results in a thinner, more inhomogeneous CEI layer accompanied by enhanced Ni dissolution. Furthermore, NCM90 at a highly delithiated state promotes the release of reactive oxygen species, which react with the electrolyte and evolve gases such as CO_2 and CO. These degradation phenomena are primarily surface-localized; the NCM90 cathode maintains its structural and electrochemical integrity in the bulk.

The evolutions of the SiO_x@Gr anode after overcharging are more significant and complex, several key trends including: (1) Elevated temperature accelerates electrolyte decomposition, leading to SEI thickening both on graphite and SiO_x particles. Concurrently, organic components within the pre-existing SEI undergo thermal decomposition, releasing gas and increasing the inorganic content of the interphase. (2) Excess Li^+ ions migrate from cathode to anode, where part intercalates into SiO_x, inducing repeated volume expansion and promoting crack formation both on the surface and in the bulk. Another fraction fails to intercalate into graphite, likely due to thermally driven side reactions that promote the conversion of LiC_6 to LiC_{12}. These side reactions exacerbate graphite polarization and facilitate lithium plating on its surface. Critically, graphite and SiO_x exhibit cross-component interactions: Rising voltage/temperature during overcharge triggers LiC_6-to-LiC_{12} phase transition and active Li^+ loss in graphite. Li^+ subsequently diffuses into adjacent SiO_x particles,[46] creating a heterogeneous Li^+ distribution within SiO_x that induces non-uniform stress and initiates internal particle cracking. (3) Dissolved Ni ions (predominantly Ni^{2+}) deposit preferentially on lithium-plated regions of the graphite anode. The deposited Ni ions on the SiO_x@Gr composite anode further catalyze the decomposition of lithium salts.[51]

These results demonstrate that in 360 Wh kg^{-1} high-energy-density pouch cells, failure of the SiO_x@Gr composite anode, mainly characterized by lithium plating on graphite and fracture

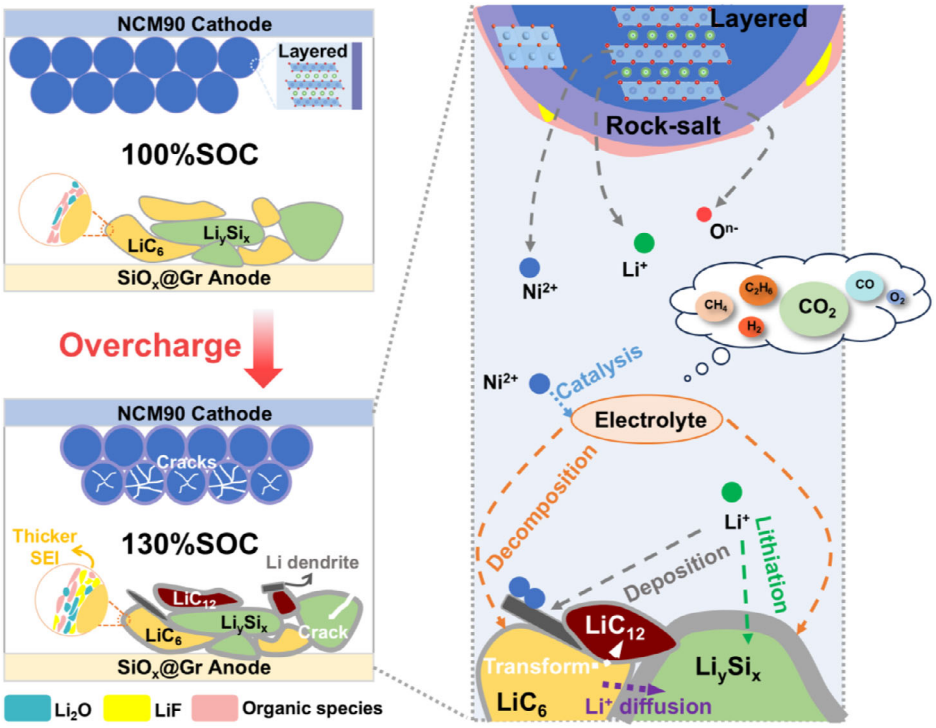

Figure 5. Schematic image for sequential evolution during the overcharge process.

of silicon-based particles, constitutes the primary mechanism of cell failure during overcharging. Exclusive Li deposition on graphite is attributed to the combined effects of enhanced side reactions at the graphite interface under elevated temperatures and altered spatial distribution of the electrochemical potential due to additional Li^+ insertion into silicon. Furthermore, the extent of graphite lithiation modulates Li^+ diffusion kinetics toward silicon particles, influencing their stress distribution and ultimately leading to crack initiation. These cross-component interactions are markedly exacerbated at higher silicon ratios. Consequently, suppressing lithium plating on graphite, optimizing the graphite interface,[54] or improving the composite architecture between graphite and silicon[55] is essential to enhancing anode stability. Moreover, the severe Ni dissolution issue in Ni-rich cathodes not only accelerates structural degradation and active material loss at the cathode but also allows dissolved Ni to migrate and deposit on the anode. This deposition catalyzes electrolyte decomposition and compromises SEI stability. Strategies like surface coatings or doping on high-nickel cathodes can suppress structural degradation and TM dissolution,[56,57] thereby improving battery safety.

4. Conclusion

In summary, multiscale investigation systematically unveils the structural and interfacial degradation mechanisms of 360 Wh kg^{-1} NCM90||SiO_x@Gr pouch cells under overcharging conditions, confirming that the decline in battery performance mainly results from the structural instability of the SiO_x@Gr anode and the synergistic deterioration effect between the cathode and anode. During overcharging, the dominant causes of the anode failure were lithium plating on the graphite surface (evolving from nano-dendrites at 110%SOC to micron-scale clusters at 130%SOC) and crack propagation in SiO_x particles with surface corrosion layer thickening. This deterioration was attributed to the reaction of LiC_6 with the electrolyte at high temperature and the additional lithium intercalation into silicon (originating from either the cathode or graphite). Additionally, Ni^{2+} dissolved from the cathode deposits on the lithium-plated areas of the graphite surface, which catalyzes electrolyte decomposition and LiF-rich SEI growth. Although the increased Li/Ni mixing caused surface rock-salt phase thickening and propagation of intergranular cracks from the bulk to the surface, the capacity of the NCM90 cathode remained minimally affected. However, the reaction between the released oxygen species and the lithiated graphite promoted the gas release and the degradation of the electrochemical performance, which emphasized the effect of the crosstalk in the full cell. These findings establish a theoretical basis for defining critical overcharge thresholds in battery management systems, with voltage change rate ($\Delta V/\Delta t$) and temperature change rate ($\Delta T/\Delta t$) emerging as the most robust and actionable early warning indicators for pack-level protection.

Supporting Information

Supporting Information is available from the Wiley Online Library or from the author.

Acknowledgements

S.L. and Y.W. contributed equally to this work. This work was supported by the National Key Research and Development Program of China (Grant

No. 2022YFB2502200), the National Natural Science Foundation of China (NSFC Nos. 52172257), the China Postdoctoral Science Foundation (No. 2024M762391) and Jiangsu Funding Program for Excellent Postdoctoral Talent.

Conflict of Interest

The authors declare no conflict of interest.

Author Contributions

X.W., S.L., and Y.W. conceived the idea and designed the project. A.Z. analyzed the EIS spectra. Z.L. conducted partial cryo-TEM characterization. G.C., Q.Y., W.L., and H.Y. provided the batteries needed for the experiment. S.L., and Y.W. performed all the other data collection and analysis. A.Z., G.C., Q. Y., W. L., H.Y., X.C. Y.W., and H.L. contributed to discussions and interpretation of results. X.W., H.L., and S.L. co-wrote the manuscript, with input from all authors.

Data Availability Statement

The data that support the findings of this study are available from the corresponding author upon reasonable request.

Keywords

failure mechanism, interfacial degradation, lithium-ion battery, overcharge

Received: September 17, 2025
Revised: November 11, 2025
Published online:

[1] T. Zhang, J. Yu, H. Guo, J. Qi, M. Che, M. Hou, P. Jiao, Z. Zhang, Z. Yan, L. Zhou, K. Zhang, J. Chen, *Chem. Soc. Rev.* **2024**, *53*, 12043.
[2] S. Link, L. Schneider, A. Stephan, L. Weymann, P. Plötz, *Nat. Energy* **2025**, *10*, 526.
[3] H. Du, Y. Wang, Y. Kang, Y. Zhao, Y. Tian, X. Wang, Y. Tan, Z. Liang, J. Wozny, T. Li, D. Ren, L. Wang, X. He, P. Xiao, E. Mao, N. Tavajohi, F. Kang, B. Li, *Adv. Mater.* **2024**, *36*, 2401482.
[4] J. Xie, Y. C. Lu, *Adv. Mater.* **2024**, *37*, 2312451.
[5] C. Xu, B. Peng, W. Yang, J. Tian, H. Zhou, *Chem. Soc. Rev.* **2025**, *54*, 10245.
[6] J.-H. Kim, N.-Y. Kim, Z. Ju, Y.-K. Hong, K.-D. Kang, J.-H. Pang, S.-J. Lee, S.-S. Chae, M.-S. Park, J.-Y. Kim, G. Yu, S.-Y. Lee, *Nat. Energy* **2025**, *10*, 295.
[7] W. Yao, K. Liao, T. Lai, H. Sul, A. Manthiram, *Chem. Rev.* **2024**, *124*, 4935.
[8] Y. Zhang, Y. Zhang, X. Wang, H. Gong, Y. Cao, K. Ma, S. Zhang, S. Wang, W. Yang, L. Wang, J. Sun, *Adv. Energy Mater.* **2024**, *15*, 2403751.
[9] S. Chen, G. Zheng, X. Yao, J. Xiao, W. Zhao, K. Li, J. Fang, Z. Jiang, Y. Huang, Y. Ji, K. Yang, Z.-W. Yin, M. Zhang, F. Pan, L. Yang, *ACS Nano* **2024**, *18*, 6600.
[10] X. Zhuang, S. Zhang, Z. Cui, B. Xie, T. Gong, X. Zhang, J. Li, R. Wu, S. Wang, L. Qiao, T. Liu, S. Dong, G. Xu, L. Huang, G. Cui, *Angew. Chem., Int. Ed.* **2023**, *63*, 202315710.
[11] M. Bai, X. Tang, M. Zhang, H. Wang, Z. Wang, A. Shao, Y. Ma, *Nat. Commun.* **2024**, *15*, 5375.
[12] Z. Cui, A. Manthiram, *Angew. Chem., Int. Ed.* **2023**, *62*, 202307243.
[13] P. Liu, L. Yang, B. Xiao, H. Wang, L. Li, S. Ye, Y. Li, X. Ren, X. Ouyang, J. Hu, F. Pan, Q. Zhang, J. Liu, *Adv. Funct. Mater.* **2022**, *32*, 2208586.
[14] R. Sim, L. Su, A. Dolocan, A. Manthiram, *Adv. Mater.* **2023**, *36*, 2311573.
[15] G. Qian, Y. Li, H. Chen, L. Xie, T. Liu, N. Yang, Y. Song, C. Lin, J. Cheng, N. Nakashima, M. Zhang, Z. Li, W. Zhao, X. Yang, H. Lin, X. Lu, L. Yang, H. Li, K. Amine, L. Chen, F. Pan, *Nat. Commun.* **2023**, *14*, 6048.
[16] Q. Fang, S. Xu, X. Sha, D. Liu, X. Zhang, W. Li, S. Weng, X. Li, L. Chen, H. Li, B. Wang, Z. Wang, X. Wang, *Energy Environ. Sci.* **2024**, *17*, 6368.
[17] J. Tao, L. Liu, J. Han, J. Peng, Y. Chen, Y. Yang, H.-R. Yao, J. Li, Z. Huang, Y. Lin, *Energy Storage Mater.* **2023**, *60*, 102809.
[18] Q. Guo, S. Liu, J. Zhang, Z. Huang, D. Han, *J. Power Sources* **2024**, *600*, 234237.
[19] Y. Song, L. Wang, L. Sheng, D. Ren, H. Liang, Y. Li, A. Wang, H. Zhang, H. Xu, X. He, *Energy Environ. Sci.* **2023**, *16*, 1943.
[20] Q. Wang, B. Mao, S. I. Stoliarov, J. Sun, *Prog. Energy Combust. Sci.* **2019**, *73*, 95.
[21] Y. Wang, X. Feng, W. Huang, X. He, L. Wang, M. Ouyang, *Adv. Energy Mater.* **2023**, *13*, 2203841.
[22] S. Jo, S. Seo, S. K. Kang, I. Na, S. Kunze, M. Song, S. Hwang, S. P. Woo, S. Kim, W. B. Kim, J. Lim, *Adv. Mater.* **2024**, *36*, 2402024.
[23] Y. S. Meng, V. Srinivasan, K. Xu, *Science* **2022**, *378*, abq3750.
[24] G. Zhang, X. Wei, J. Zhu, S. Chen, G. Han, H. Dai, *J. Power Sources* **2022**, *543*, 231867.
[25] X. Feng, D. Ren, X. He, M. Ouyang, *Joule* **2020**, *4*, 743.
[26] C. Xu, Z. Fan, M. Zhang, P. Wang, H. Wang, C. Jin, Y. Peng, F. Jiang, X. Feng, M. Ouyang, *Cell Rep. Phys. Sci.* **2023**, *4*, 101705.
[27] J. Liu, Q. Duan, L. Feng, M. Ma, J. Sun, Q. Wang, *J. Energy Storage* **2020**, *29*, 101397.
[28] S. Xie, Y. Gong, X. Ping, J. Sun, X. Chen, Y. He, *J. Energy Storage* **2022**, *46*, 103829.
[29] H. Zhang, Y. Peng, Y. Hu, S. Pan, S. Tang, Y. Luo, Y. Liang, Y. Liao, Y. Lin, K. Zhang, Y. Wei, J. Liang, Y. Jin, Y. Yang, *Adv. Energy Mater.* **2025**, *15*, 2404997.
[30] B. Rowden, N. Garcia-Araez, *Energy Rep.* **2020**, *6*, 10.
[31] C. Qi, Y.-l. Zhu, F. Gao, K. Yang, Q.-j. Jiao, *J. Electrochem. Soc.* **2018**, *165*, A3985.
[32] D. Ren, X. Feng, L. Lu, M. Ouyang, S. Zheng, J. Li, X. He, *J. Power Sources* **2017**, *364*, 328.
[33] C. Yang, A. Singh, X. Pu, A. Mallarapu, K. Smith, M. Keyser, M. R. Haberman, H. Khani, P. Misztal, R. Spray, O. A. Ezekoye, D. P. Finegan, *Nature* **2025**, *645*, 603.
[34] Y. Yan, F. Hai, B. Wang, W. Cao, M. Li, C. Wang, N. Li, D. Zhao, *Energy Storage Mater.* **2025**, *79*, 104312.
[35] K. Wu, P. Ran, W. Yin, L. He, B. Wang, F. Wang, E. Zhao, J. Zhao, *Angew. Chem., Int. Ed.* **2024**, *63*, 202410326.
[36] B. L. D. Rinkel, J. P. Vivek, N. Garcia-Araez, C. P. Grey, *Energy Environ. Sci.* **2022**, *15*, 3416.
[37] T. Waldmann, B.-I. Hogg, M. Wohlfahrt-Mehrens, *J. Power Sources* **2018**, *384*, 107.
[38] Y. Fernandes, A. Bry, S. de Persis, *J. Power Sources* **2018**, *389*, 106.
[39] R. Jung, M. Metzger, F. Maglia, C. Stinner, H. A. Gasteiger, *J. Electrochem. Soc.* **2017**, *164*, A1361.
[40] E. W. C. Spotte-Smith, S. Vijay, T. B. Petrocelli, B. L. D. Rinkel, B. D. McCloskey, K. A. Persson, *J. Phys. Chem. Lett.* **2024**, *15*, 391.
[41] R. Jung, M. Metzger, F. Maglia, C. Stinner, H. A. Gasteiger, *J. Phys. Chem. Lett.* **2017**, *8*, 4820.
[42] J. Wandt, A. T. S. Freiberg, A. Ogrodnik, H. A. Gasteiger, *Mater. Today* **2018**, *21*, 825.
[43] J. Wu, S. Weng, X. Zhang, W. Sun, W. Wu, Q. Wang, X. Yu, L. Chen, Z. Wang, X. Wang, *Small* **2023**, *19*, 2208239.
[44] X. Wang, D. Ren, H. Liang, Y. Song, H. Huo, A. Wang, Y. Gao, J. Liu, Y. Gao, L. Wang, X. He, *Energy Environ. Sci.* **2023**, *16*, 1200.
[45] M. Metzger, B. Strehle, S. Solchenbach, H. A. Gasteiger, *J. Electrochem. Soc.* **2016**, *163*, A798.

[46] Y. Zhang, W. P. Wang, Y. Zhao, X. Zhang, H. Guo, H. Gao, D. X. Xu, Y. M. Zhao, G. Li, J. Y. Liang, S. Xin, Y. G. Guo, *Adv. Funct. Mater.* **2023**, *34*, 2310309.
[47] C. Cao, T. P. Pollard, O. Borodin, J. E. Mars, Y. Tsao, M. R. Lukatskaya, R. M. Kasse, M. A. Schroeder, K. Xu, M. F. Toney, H.-G. Steinrück, *Chem. Mater.* **2021**, *33*, 7315.
[48] H. Xu, Z. Li, T. Liu, C. Han, C. Guo, H. Zhao, Q. Li, J. Lu, K. Amine, X. Qiu, *Angew. Chem., Int. Ed.* **2022**, *61*, 202202894.
[49] S. K. Heiskanen, J. Kim, B. L. Lucht, *Joule* **2019**, *3*, 2322.
[50] J. Zhang, S. Weng, C. Zhong, J. Zhu, Y. Liu, Q. Fang, H. Zhang, Y. Li, X. Wang, *Adv. Mater.* **2025**, *37*, 13736.
[51] X. Zhang, Z. Cui, A. Manthiram, *Adv. Energy Mater.* **2022**, *12*, 2103611.
[52] S. Li, Z. Liu, L. Yang, X. Shen, Q. Liu, Z. Hu, Q. Kong, J. Ma, J. Li, H.-J. Lin, C.-T. Chen, X. Wang, R. Yu, Z. Wang, L. Chen, *Nano Energy* **2022**, *98*, 107335.
[53] C. Liu, S. Reed, A. Manthiram, *Adv. Mater.* **2025**, *37*, 09889.
[54] S. Chen, Z. Deng, J. Li, W. Zhao, B. Nan, Y. Zuo, J. Fang, Y. Huang, Z. W. Yin, F. Pan, L. Yang, *Angew. Chem., Int. Ed.* **2024**, *64*, 202505832.
[55] Z. He, C. Zhang, Z. Zhu, Y. Yu, C. Zheng, F. Wei, *Adv. Funct. Mater.* **2024**, *34*, 2408285.
[56] S. Pal, X. Lin, P. Apostol, C. Ungureanu, D. Tie, V. R. Bakuru, D. Rambabu, N. Campagnol, A. Kachmar, C. Poleunis, G. Barozzino-Consiglio, M. Buga, A. Vlad, *ACS Energy Lett.* **2024**, *9*, 4399.
[57] X. Zhang, P. Xu, J. Duan, X. Lin, J. Sun, W. Shi, H. Xu, W. Dou, Q. Zheng, R. Yuan, J. Wang, Y. Zhang, S. Yu, Z. Chen, M. Zheng, J.-F. Gohy, Q. Dong, A. Vlad, *Nat. Commun.* **2024**, *15*, 2041.